Design Rules for Structural Colors in All-Dielectric Metasurfaces: From Individual Resonators to Collective Resonances and Color Multiplexing

Kévin Vilayphone, Mohamed Amara, Regis Orobtchouk, Fabien Mandorlo, Serge Mazauric, Xavier Letartre, Sébastien Cueff, Hai Son Nguyen, Thomas Wood

Design rules for structural colors in all-dielectric metasurfaces : from individual resonators to collective resonances and color multiplexing

KÉVIN VILAYPHONE,[1] MOHAMED AMARA, [1] REGIS OROBTCHOUK, [1] FABIEN MANDORLO, [1] SERGE MAZAURIC,[1] XAVIER LETARTRE, [1] SÉBASTIEN CUEFF, [1,*] HAI SON NGUYEN,[1,*] AND THOMAS WOOD, [1,*]

[1]*Univ Lyon, Ecole Centrale de Lyon, CNRS, INSA Lyon, Université Claude Bernard Lyon 1, CPE Lyon, INL, UMR5270, 69130 Ecully, France*
[*] sebastien.cueff@ec-lyon.fr, hai-son.nguyen@ec-lyon.fr, thomas.wood@insa-lyon.fr

Abstract
In this work, we comprehensively review Mie resonator based and non-local resonant metasurfaces working in the reflection configuration for color printing applications, with particular attention to high observation angle applications. Whilst Mie resonator based metasurfaces are found to be simple to design and present low sensitivity to the observation angle, they present the drawback of low color saturation. By contrast, square lattice photonic crystal waveguide based metasurfaces show very selective spectral responses yielding pure colors but with high selectivity on the observation angle. In order to harness the exceptional color filtering properties of photonic crystal waveguides and maintain the wanted spectral response under oblique angles of observation, a rectangular lattice for the crystal structure is proposed. We provide design rules and examples in order to produce angularly robust, vivid colors at any desired wavelength within the visible spectrum. Furthermore, by exploiting the polarization of the incident light and adapting the design of the photonic crystal structures, we demonstrate color multiplexing for cryptography applications.

Introduction

Structural color is a coloration phenomenon that can be observed in nature, for example in peacocks' tails or *Morpho* butterflies' wings (1). Systems displaying structural color are composed of periodic arrays of nanoscale objects which interact with incident light and produce interferences or resonances that are responsible for the color we see (1). Advances in nanotechnology now make it possible to create artificial surfaces textured by nanostructures for which the characteristic length scale is below the wavelength of visible light. The creation of artificial structural color based on metasurfaces has therefore been strongly developed over the last few years (2,3,4,5,6). The first works on the subject focused on plasmonic resonances with metallic structures (7,8,9,10,11,12,13,14) but optical losses due to the use of metal, as well as unsaturated colors due to low resonance quality factors were observed (15).

Recently, research in the field of structural color has been focused on all-dielectric surfaces (16,17,18,19,20,21,22,23,24,25,26,27) based on materials with high refractive indices but that are transparent in the visible wavelength range like Si_3N_4 or TiO_2. This approach leads to brighter colors with less optical loss (15), and has many fields of application (2,15,18,28,29,30,31). The structural colors obtained in the reflection configuration with these metasurfaces (32) can be divided into two categories: on the one hand there are systems exploiting effects observed in individual resonators in so called "local metasurfaces", based on Mie resonances, where the nanostructures host multipolar electric or magnetic resonances (2,33). Such systems have many assets: they have high spatial resolution due to their subwavelength size and the fact that each resonator acts independently; furthermore, unlike simple planar stacks, they are virtually independent of the angle of observation. However, drawbacks include

low spectral resolution due to low resonance quality factors and reflectivities that do not reach unity (34) in part due to low interaction cross sections often related to poor surface coverage. On the other hand, there are structural colors based on the principles of collective resonances in so-called photonic crystals, or "non-local metasurfaces". Such collective, or "Bloch", resonances are generated by sub-wavelength periodic arrays of holes in a planar dielectric layer or free-standing pillars (35,36). Contrary to the individual Mie resonators, photonic crystals offer a high spectral resolution with high resonance quality factors (15,20,37). The linewidth can reach below 10 nm which is the same order of magnitude as the linewidth of the luminescence spectrum of quantum dots used in QLED technology (38,39). However, the spatial resolution is worse than the individual resonator approach because it requires several resonators, i.e. a few periods, to obtain a collective effect. Nonetheless, the overall structure size is only a few microns per side which compares favorably to the pixel size in an 8K screen, being of the order of a few hundred microns per side (~100 PPI, or pixels per inch).

The major weak point of collective resonance-based systems is the strong dependence on the observation angle due to the diffractive origins of the resonances. This angular dependence is all the more important in systems exploiting advanced properties of photonic crystals, such as quasi-bound states in the continuum (q-BICs) displaying high quality factor resonances in asymmetric photonic crystal (PC) structures, in order to reduce the spectral linewidth of the reflected peaks at the desired operating wavelengths and suppress those at neighboring wavelengths. We note that such techniques are often needed to produce pure red colors, which are typically difficult to obtain due to the presence of higher order resonant modes that typically exist at shorter wavelengths falling within the visible spectral region. In reference (40), the authors exploit two q-BIC modes of a two-dimensional PC structure with partial spectral overlap in order to create an isolated reflectance pedestal, giving exceptional performance in the CIE color space with coordinates outside the RGB triangle and yielding a so-called Schrödinger's red pixel. However, the angular sensitivity of the q-BIC modes led to severely degraded performances as the observation angle increases, with the authors citing a limiting operation angle of 6.9°. The issue of angle of incidence restriction - and the corresponding limitation of observation angles for display applications - is also present in thin-film (41) and liquid crystal-based (42,43) color pixels, due to their operation principal based on optical path length in the different layers of the device. Whilst for 'traditional' displays such as television screens or computer monitors it is necessary to ensure they can be viewed in oblique incidence (as would be the case when many observers are watching the same display in close proximity), in other devices such as virtual/augmented reality systems – designed to be mounted in headsets directly in front of the observer – the observation angle range is constrained to only a few degrees around normal incidence. For this reason, we note that it is impossible to specify a minimum acceptable observation angle, below which color pixel technologies must all function, as such a limit is completely dependent on the intended application. In this work, so as to open up as many applications as possible, we seek to create color pixels whose spectral response is independent on the observation angle over as wide a range as possible.

In the following, we make a comprehensive study of structural color in all-dielectric metasurfaces, and use them to show polarization sensitive color filters with robust angular responses. First of all, we perform a benchmark comparison between the Mie resonator and photonic crystal approaches by comparing the colors obtained with individual dielectric resonators and those produced by the same resonators arranged in periodic arrays. Next, we focus on the use of photonic crystals and propose a method which uses engineering of band diagrams to isolate and spectrally control resonances that show little dependence on the angle of observation, representing a rupture with the literature for PC based metasurfaces. Finally, we propose structural color multiplexing which can display different colors and messages with the same static metasurface, just by changing the polarization of the incident light. Such polarization sensitive metasurfaces have applications in critical domains such as information security and anti-counterfeiting (44). In contrast to existing examples in the literature of polarization-sensitive metasurfaces (45,46,47,48,49,50,51), the approach presented here allows us to employ symmetrical resonators

(cylinders in this case) and achieve a polarization dependent response by simply setting a different period of the PC structure in the two orthogonal directions in the substrate plane. This approach therefore relaxes the fabrication constraints by reducing the critical dependence of the polarization response on the shape of individual resonators, which can be anisotropically influenced in an uncontrollable fashion by fabrication processes such as etching.

Results and discussion

Design

The following designs are based on TiO_2; the most widely used material for all-dielectric metasurfaces in the visible wavelength range (2,3,15,52) due to its high refractive index and its transparency in this spectral region (2,3,15). The refractive index of the material was obtained through ellipsometry measurements performed on a sputtered thin film of TiO_2. In the following, all the simulations are carried out in a non-dispersive framework, the refractive index of the TiO_2 chosen being the average obtained over the visible wavelength range, which is $n_{TiO2} = 2.633$ and a negligible extinction coefficient $k_{TiO2} = 0$. We underline here that this paper is destined to provide a general method for designing structural color metasurfaces, and as such the exact dispersion characteristics of the material given as an example in this study, namely TiO_2, are unimportant. The design is composed of cylindrical TiO_2 nanopillars periodically arranged on a SiO_2 substrate of which the refractive index is taken as $n_{SiO2} = 1.470$. As shown in Figure 1, d represents the diameter of the pillars and h represents their height, whilst a_x and a_y are the lattice periods along x-axis and y-axis. Finally, the angles describing the direction of incident light are θ measured in the plane of incidence from the z-axis, and ϕ describing the orientation of the plane of incidence from the x-axis. The angle ϕ is typically set to zero in our study, and is only varied where clearly specified in order to verify the robustness of the colors produced.

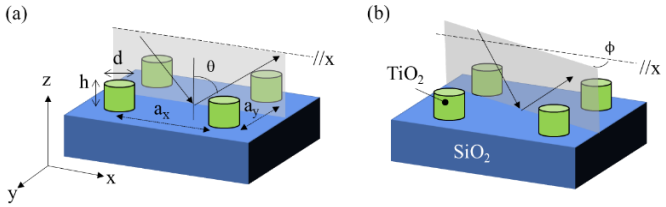

Figure 1 – The design with cylindrical nanopillars used in this work. (a) Showing coordinate system, studied parameters and defining the incidence angle θ. (b) Showing materials used and defining incidence angle ϕ. The plane of incidence is shown in gray.

The following sections are devoted to benchmarking the two approaches; firstly individual resonators, followed by those coupled in photonic crystal structures, in their use to engineer vivid reflected colors. The simulations were carried out with finite difference time domain (FDTD) calculations for the Mie resonators (Lumerical commercial solver) and with rigorous coupled wave analysis (RCWA) for the photonic crystal structures (S4 freeware and in-house code).

Structural colors from Mie resonances in individual pillars

First, we focus on the study of the Mie resonances of individual cylinders by setting the height h and varying their diameter. Figure 2 (a-c) show 2D mappings of the scattering cross section of single resonators as a function of the diameter d and the wavelength, and reveal the resonant modes of the cylinders which begin with dipolar magnetic (MD) and electric (ED) resonances at high wavelengths before encompassing higher order (eg. quadripolar) resonances as the wavelength decreases. Figure 2 (d-f) show normalized specular reflection spectra for such nanopillars, when illuminated with a diffraction-limited gaussian beam (waist radius = 0.5μm, beam divergence = 15°) normal to the substrate, for a variety of cylinder heights h. This parameter is calculated by projecting the backscattered optical power into the far-field and summing all power within 15° of the normal axis of the surface before

normalizing to the highest value of reflected power at any wavelength, and should therefore be thought of as a reflection coefficient for confocal excitation and collection with the same lens. The apparent color of the structure when observed in such conditions and its coordinates in the CIE gamut, in which the outer curved boundary corresponds to monochromatic colors (53), can be extracted via ponderation of the spectra in Figure 2 (d-f) with the three color-matching functions (33), as shown in Figure 2 (g). From the coordinates obtained within the CIE-xy chromaticity diagram we observe that the apparent colors are very desaturated due to the presence of a high background baseline in the normalized reflectance spectra and multiple, broad resonance peaks. Therefore, high-volume pillars under white light excitation respond simultaneously to multiple wavelengths, desaturating their apparent colors. Care must also be taken when considering the intensity of the reflected light, as a very low fraction of the incident power is reflected (despite the near-matching of the gaussian beam's diameter to that of the resonators), with this metric not being displayed in the CIE-xy chromaticity diagram. By way of example, for the largest resonator considered (h=300, d=400nm), the wavelength-averaged total power reflected into the upper half plane (i.e. above the substrate) is around 15%.

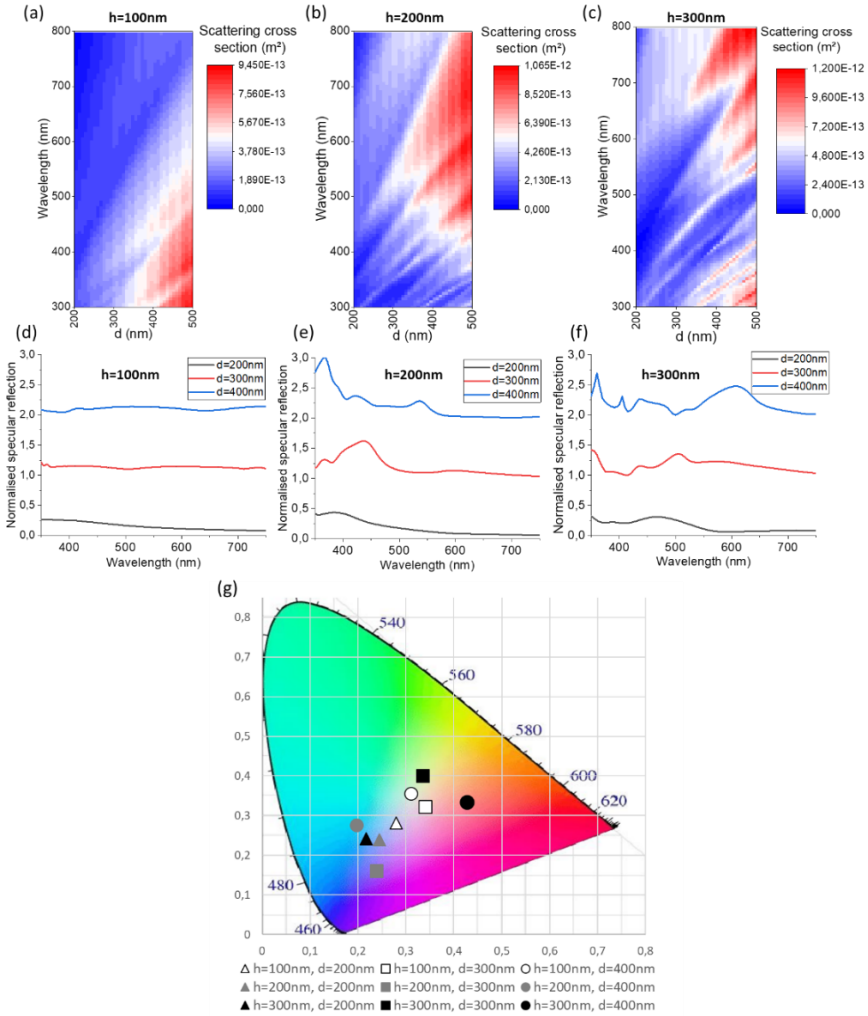

Figure 2 - (a-c) The scattering cross section of the cylindrical nanopillars for h = 100nm, h = 200nm and h = 300nm over the continuous range of diameters studied. (d-f) Normalized reflection spectra of the cylindrical nanopillars for h = 200nm, h = 300nm (shifted by one unit on y-axis) and h = 400nm (shifted by two units on y-axis) for three selected diameters as shown on each graph. (g) The CIE-xy diagram of the diffused colors for the nanopillars.

From individual resonators to collective effects

As stated earlier, many studies have been performed in the literature on the assembly of individual resonators into two-dimensional arrays known as metasurfaces, with one resonator per unit cell of the array. Furthermore, it is well known from diffraction theory that if the period of such an array is below the wavelength of incident light, only a specularly reflected beam will exist (i.e. there will be no diffracted orders) in free space on the side of the metasurface from which the light was incident (54). It has been shown in the literature that in such configurations the angular distribution of energy scattered by individual resonators can determine the overall polarization response of the metasurface, that is to say the intensity of light channeled into the specularly reflected beam can be conditioned by the angularly resolved scattering cross section of each individual resonator. This has been used to demonstrate a so-called Generalized Brewster effect in metasurfaces (55). We note that the angular dependence of the scattering has its origins in near-field distribution of the optical energy in the resonant Mie modes and the relative phases of the underlying electric and magnetic fields, which condition the far-field radiation pattern when different types of mode (eg. ED and MD) overlap spectrally.

When the period of the array becomes sufficiently small for neighboring resonators to interact through overlap of their resonant fields, new physics comes into play. It has been shown that Mie modes in individual resonators can couple to non-local modes spread across the array whose spectral position can be fine-tuned by adjusting the array period. Such coupling occurs if the spectral position and the near-field energy distributions of the two types of mode (Mie and non-local) overlap, and can lead to anomalous reflection and transmission phenomena such as the so-called Resonant Lattice Kerker Effect (56).

Structural colors from collective effects in Photonic Crystals

In this work, we will work in the case of non-local metasurfaces, where the individual resonators are coupled through their near-fields. However, rather than considering the system as being an assembly of Mie resonators, we will take a macroscopic view and describe the system as a slab photonic crystal. Such systems, often called photonic crystal waveguides (PCWG), may be visualized conceptually as a waveguide with an integrated coupling structure, allowing coupling between the waveguided modes, generating Bloch modes, and exchanges of photons with free space. A basic, planar waveguide structure (SiO_2 substrate, TiO_2 guiding layer, air cladding) may be used as a starting point in order to design the structuration needed to give narrow resonant reflection peaks at a desired operating wavelength. Such peaks have their physical origin in the diffractive coupling of photons from free space into guided modes, followed by their subsequent re-emission having gathered a well-defined phase shift that ensures constructive interference with light reflected on the top surface of the structure.

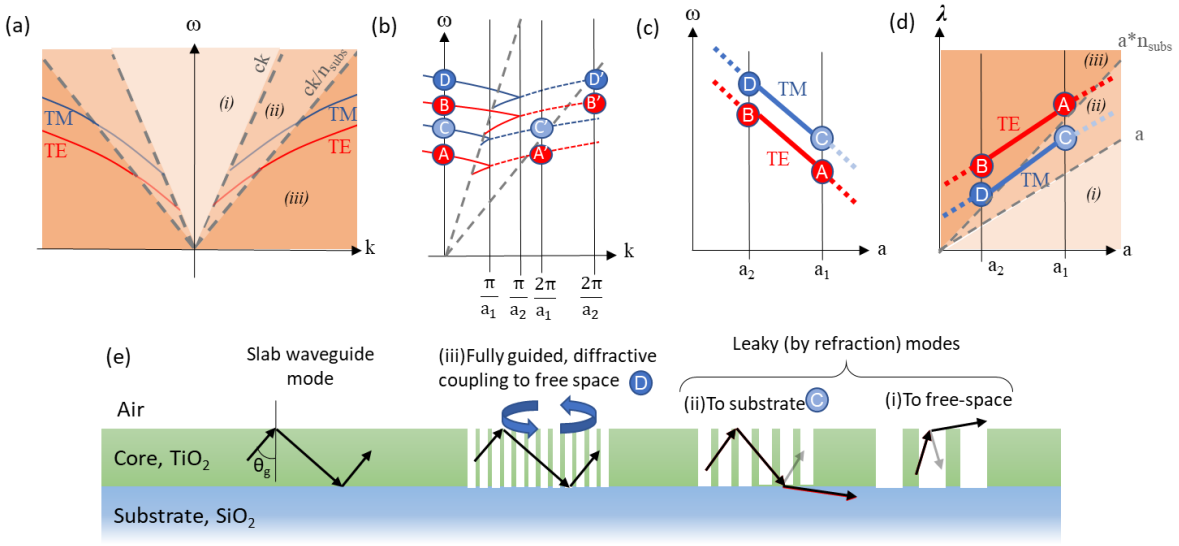

Figure 3 – (a) Band diagram for a slab waveguide, showing the dispersion curves one mode per polarization (TE and TM) and the regions corresponding to (i) modes that leak by refraction to air, (ii) modes that leak by refraction to the substrate, and (iii) fully confined modes that interact with free space by diffraction. (b) Band diagram for one dimensional PCWGs with two different periods, a_1 and a_2, with central crossing points (k=0) labelled (A-D) for reference in other panels. The folding of the band diagram ensures that the frequencies of the central crossing points are those of the original modes at $k=2\pi/a_{1,2}$ (points labeled A' – D'). Note that the mode with central crossing point C is a leaky mode to the substrate, as at $k=2\pi/a_1$ (i.e. at point C') it is in region (ii). (c) Translation of frequencies corresponding to central crossing points onto a diagram showing frequencies of allowed modes as a function of period, when the PCWG structure is illuminated in normal incidence. (d) as (c) but with conversion of frequency to wavelength to match the presentation of the reflectivity diagrams in Figure 6 and Figure 8. (e) Representation of guided modes in the different regimes (i), (ii) and (iii) detailed previously, showing qualitatively the dependence of the regimes on the structuration period (high to low from i) to iii) respectively).

Initially, the thickness of the un-patterned, planar waveguide structure is set such that light reflected at the cladding/waveguide interface interferes destructively with light reflected at the waveguide/substrate interface, following the well-known Fabry-Perot mechanism for thin films. This ensures a minimal background reflection (close to R=0) onto which the reflectance peak is superimposed, and entails setting the thickness h of the waveguide to $\lambda_c/(2n_0)$, where λ_c is the central wavelength around which the reflectance peaks are required (here λ_c = 550 nm, taken by way of example due to it being in the center of the visible spectral region) and n_0 the refractive index of the waveguide (2.633), yielding h = 104 nm ≈ 100 nm.

Next, using a mode-solving algorithm, the propagation constant – that is the component of the wavevector in the plane of the substrate ($k_{//} = (2\pi/\lambda_0)\, n_0 sin\theta_g$, where θ_g is the propagation angle of the mode within the waveguide, as depicted in Figure 3(e)) – of the guided modes are calculated in the planar stack. A schematic representation of the results is shown in Figure 3 (a), where the guided modes appear in a band diagram plotting the allowed frequencies as a function of the in-plane wavevector. Only modes that fall in region (iii) of the band diagram, that is below the light-line defined by the substrate refractive index, are fully confined within a slab waveguide, whilst those in region (ii) between the air and substrate light lines are leaky to the substrate.

We now consider introducing a one-dimensional perturbation to the waveguide in order to form a 1D PCWG, resulting in a folding of the band structure that is constrained within the first Brillouin zone as shown in Figure 3 (b), bringing the guided modes above the light line and allowing them to interact with plane waves in free space. This forms a diffraction grating at the surface of the waveguide, for which the

so-called grating vector $G = 2\pi/a$ must be equal to the propagation constant of a guided mode at the wavelength at which a reflectance peak is required, λ_p, so that a normally incident plane wave from free space can couple to the mode on the first diffracted order of the grating. In the band diagram of Figure 3 (b), this corresponds to the guided mode curve crossing the center of the diagram ($k_{//} = 0$) at λ_p.

Given that the extension of the first Brillouin zone depends on the periodicity a, the frequencies (or wavelengths) corresponding to crossing points of $k_{//} = 0$ for the guided mode curves depend on the periodicity, as can be seen in Figure 3 (c) (and (d)). Reformulating for a give us the starting point for the range of periodicities to explore in order to produce the required color of the reflectance peak. In the present case, for a coupling to the TE guided mode at $\lambda_p = 550$ nm to form a green pixel, we need a periodicity $a = 250$ nm, which ensures since $a < \lambda_p$ that no diffracted orders propagate in free space and that the obtained light is specularly reflected. We note that, given that the PCWG is formed by removing material from the planar waveguide in order to produce the grating and that such an action reduces the effective optical thickness of the waveguide, this value for the period is in fact an absolute minimum.

We must now optimize the nature of the modulation to be applied to the waveguide in order to maximize the amplitude of the reflectance peak and minimize its spectral width for a 'purer' color, i.e. one situated near the outer contour of the CIE diagram. It is not immediately obvious how to proceed, as a stronger modulation will allow for a greater degree of coupling with free space but will also induce losses in the waveguide, thereby reducing the quality factor of the resonances obtained and increasing the width of the reflectance peak. In order to address this problem, a parameter sweep for a 1D grating has been performed, the results of which are transposable to the 2D case studied later, where the waveguide thickness, the structuration depth (measured from the surface) and the lateral duty cycle (or filling factor) have been varied. For each parameter combination, the reflectance spectrum (R) is calculated, the reflectance peak identified (constrained within +/- 5 nm of the required wavelength λ_p), and a figure of merit FOM is constructed based on the summit of the reflectance peak:

$$FOM = -\left.\frac{d^2R}{d\lambda^2}\right|_{R_{peak}} \cdot \frac{R_{peak}}{\sum R_{global}}$$

Equation 1

The first term in Equation 1 describes the spectral finesse of the peak, whilst the second gives its dominance over the off-resonant background reflection spectrum $\sum R_{global}$, i.e. the average reflectance over the full wavelength range considered (ranging from $0.95 < \lambda/\lambda_p < 1.15$, or around $500 < \lambda < 630$ nm for the case $\lambda_p = 550\ nm$). The FOM is averaged for 5 wavelength points around the peak maximum, where the simulation wavelength step is 1 nm. Figure 4 (a) shows the normalized results of this sweep, where the parameters have been condensed into the duty cycle *dc* and a vertical etching factor *fev*, the latter representing the fraction of the total waveguide depth that is occupied by the modulation (0 = un-modulated waveguide, 1 = fully etched grating elements) as shown in Figure 4 (d). The normalization is performed by dividing all FOM values by the single maximum value.

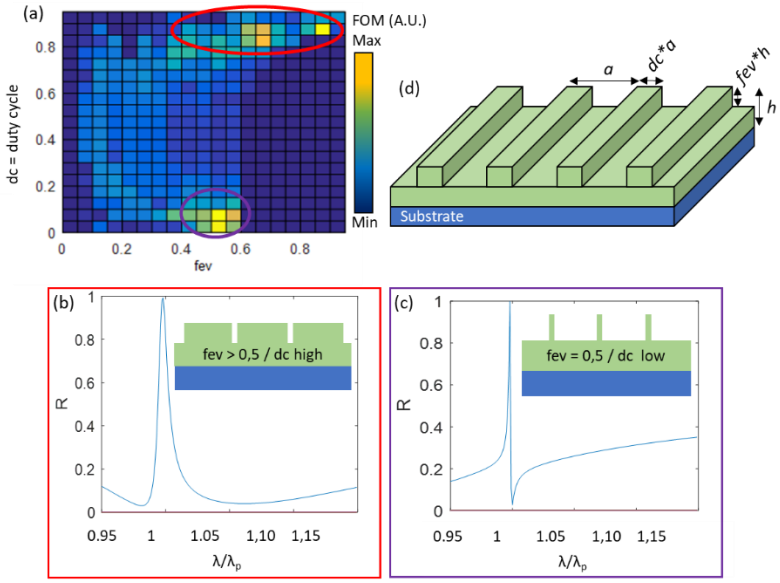

Figure 4 – (a) Normalized FOM calculated for different 1D PCWG structures as a function of the vertical etching factor *fev* and the lateral duty cycle *dc*. Normalization performed by dividing all FOM values by the single maximum value. (b)(c) representations of optimal values of the FOV as encircled in (a) in red, purple respectively. (d) Schematic of the system studied, showing the definitions of the parameters *dc* and *fev*.

It can be seen that the optimum values fall in a crescent-shaped region in the parameter space, and that intermediate values of the duty cycle are to be avoided. Two distinct possibilities for optimized reflectance peaks appear: either for low duty cycles and half-depth etching (*fev*=0.5) yielding structures depicted in Figure 4 (c), or for high duty cycles and near full-depth etching (*fev* → 1) as depicted in Figure 4 (b), with the second possibility imposing fewer constraints from a fabrication point of view (no high aspect ratio structures). We note also that the reflectance peaks in two spectra shown in Figure 4 (b,c) have very different line shapes, the origins of which are discussed in the Supplementary Information.

To extend the study to the two-dimensional situation corresponding to the nanopillars, we conserve the same parameters but note that the duty cycle is now based on the diameter of the cylindrical pillars, *dc* = *d*/*a*. Based on the previous observations, our search for reflectance peaks in the visible spectral region can be restricted to fully etched structures (*fev* =1, i.e. fully isolated pillars), high duty cycles (*dc* > 0.5), and periods *a* in excess of 250 nm. Figure 5 (a), (c) and (e) show the reflectivity spectra of the photonic crystals for *dc* fixed and *a* variable while Figure 5 (b), (d) and (f) show spectra for *a* fixed and *dc* variable, in all cases (a-f) for *h* = 100 nm, *h* = 200 nm and *h* = 300 nm. As predicted in the previous paragraphs, it can be seen that the most favorable spectral performances – confirmed by the coordinates within the CIE-xy chromaticity diagrams in Figure 5 (g) and 3(h) – are found in the case where the pillars' height h is near to 100 nm in order to minimize background reflection outside of the wanted peaks.

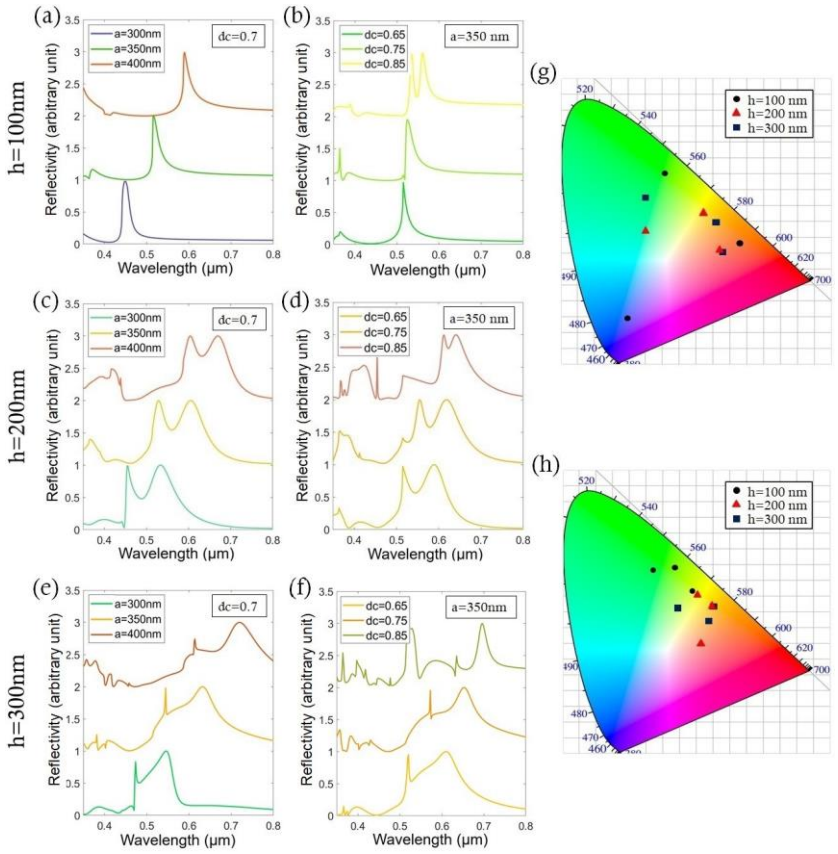

Figure 5 - (a)(b) The reflectivity spectra of the photonic crystals for *a* variable and *dc* fixed for *h* = 100nm. (c)(d) The reflectivity spectra of the photonic crystals for *a* variable and *dc* fixed for *h* = 200nm. (e)(f) The reflectivity spectra of the photonic crystals for *a* variable and *dc* fixed for *h* = 300nm. (g) The CIE-xy diagram for *a* variable and *dc* fixed. (h) The CIE-xy diagram for *dc* variable and *a* fixed.

Clearly, upon comparing Figure 2 (g) and Figure 5 (g), it can be seen that the PCWG approach offers more design possibilities and parameters which allows us to create more vivid colors than in the case of Mie resonances of individual pillars. Consequently, for the remainder of the paper, the study will be focused on photonic crystals.

Angular and polarization selectivity

Study of the different mode types in rectangular lattice PCWGs

In order to increase the angular stability of the reflectivity response and allow for polarization-selective responses from our PCWG systems, we now extend our study to rectangular lattices. We now have the periods a_x and a_y in the x and y directions respectively, giving rise to grating vector components $G_x = 2\pi/a_x$ and $G_y = 2\pi/a_y$ respectively, and we consider the x- and y-components of the in-plane wavevector $\overrightarrow{k_{//}}$ of the guided modes k_x and k_y respectively. The observation angle θ is related to the in-plane wavevector component in free space k_{x0} by the relation $k_{x0} = (2\pi/\lambda_0).\sin\theta$ and, due to the fact that there is no projection of the wavevector in free-space along y (the plane of incidence is the (xz) plane), $k_{y0} = 0$. The diffracting behavior of the PCWG in *x* (or *y*) contributes a factor m_xG_x (or m_yG_y) to the corresponding in-plane wavevector component for integer values of m_x (or m_y) called the diffracted orders. The latter is here limited to (-1,0,1) due to the low period of the PCWG so as to ensure efficient (first diffracted

order) coupling between the diffracted light in the PCWG and waves in free space. We can therefore write the total in-plane wavevector in the following way, where $\overrightarrow{u_x}$ and $\overrightarrow{u_y}$ are unit vectors along the cartesian axes:

$$\overrightarrow{k_{//}} = k_x\overrightarrow{u_x} + k_y\overrightarrow{u_y} = (k_{x0} + m_xG_x)\overrightarrow{u_x} + (m_yG_y)\overrightarrow{u_y}$$

Equation 2

Figure 6 shows the PCWGs' reflectivities as a function of the wavelength λ and the angle of observation θ in the xz plane, measured from the z axis, for an incident wave polarized with the electric field along the x-axis (E_x polarization). The origin of the bands in the reflectivity diagrams ($R(\lambda, \theta)$) and their link with those shown in typical band diagrams ($\omega(k_{//})$) is described in Figure 3. We can observe resonance bands which depend on the angle of observation and others that are independent of it, respectively termed "fast modes" and "slow modes". By analysis of Equation 2, we may conclude that the matching of wavevector components between free space and fast guided modes performed by the PCWG occurs through diffraction along x (as the wavelength at which coupling is achieved is seen to vary with θ), whilst slow modes couple with free space through diffraction along y. Indeed, the spectral position of the slow mode is seen to depend on a_y in panels (d-f) of Figure 6, whilst the fast mode's spectral positions at normal incidence (θ = 0°) depend on a_x in panels (a-c), confirming this hypothesis. The naming of the modes in Figure 6 uses the following, usual convention for guided modes in slab structures (we remind the reader that for the following argument the incident electric field was x-polarized and furthermore we limit $k_{x0} \sim 0$, that is we assume near-normal incidence): TE polarization means that no component of the electric field exists in the in-plane propagation direction y when m_y = ±1, whilst TM polarization implies the existence of components of the electric field in the in-plane propagation direction x when m_x = ±1. Extension of this reasoning to the other polarization of incident light (E_y) allows us to construct Table 1, whilst Figure 7 summarizes the different modes observable as a function of the polarization of incident light and their dispersion characteristics around the center of the first Brillouin zone where $k_x \sim 0$. For the sake of succinctness, the orthogonally polarized counterpart of Figure 6 (reflectivities of the system when illuminated under E_y polarization) is not shown here, but is available in the Supplementary Information (Figure S2). However, as expected from Figure 7 and Table 1, it should be noted that the behavior of the "slow mode", being the TM mode under E_y illumination, is exactly analogous to that of the TE mode under E_x illumination in that it remains invariant with the observation angle θ and is spectrally positioned by the choice of period a_y.

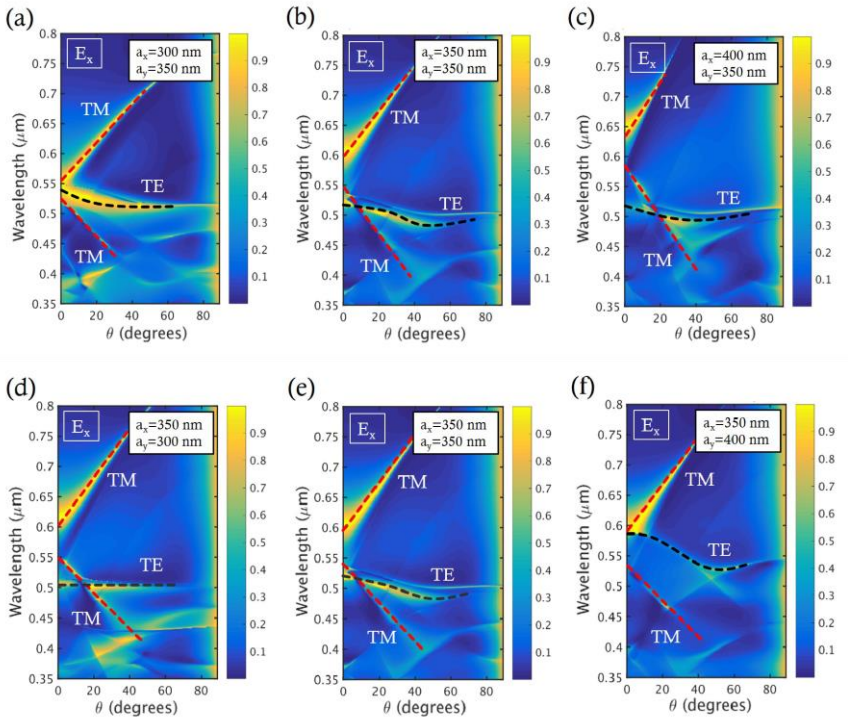

Figure 6 - The reflectivity of the photonic crystals as a function of the wavelength and the angle of observation for: (a-c) a_x variable and a_y fixed, (d-f) a_y variable and a_x fixed. For all the figures, h = 200nm, d = 240nm and the light is E_x polarized.

Slab mode polarization	$\{m_x, m_y\}$	Mode type	Dominant $\overrightarrow{k_{//}}$ component	$\vec{H}$ components	$\vec{E}$ components
TE	{±1, 0}	Fast	$\overrightarrow{u_x}$	$\overrightarrow{u_x}$, $\overrightarrow{u_z}$	$\overrightarrow{u_y}$
	{0, ±1}	Slow	$\overrightarrow{u_y}$	$\overrightarrow{u_y}$, $\overrightarrow{u_z}$	$\overrightarrow{u_x}$
TM	{±1, 0}	Fast	$\overrightarrow{u_x}$	$\overrightarrow{u_y}$	$\overrightarrow{u_x}$, $\overrightarrow{u_z}$
	{0, ±1}	Slow	$\overrightarrow{u_y}$	$\overrightarrow{u_x}$	$\overrightarrow{u_y}$, $\overrightarrow{u_z}$

Table 1 - Summary of the different modes and their properties for the PCWG illuminated under near-normal incidence, with the plane of incidence being (xz).

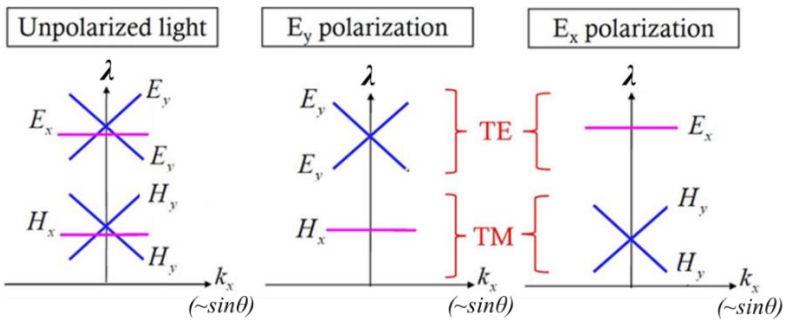

Figure 7 - The different modes which can be observed depending on the polarization of incident light.

Manipulating these different modes provokes changes in the color reflected by the photonic crystals. As said before, the main inconvenience in the photonic crystals approach is its high dependence on the angle of observation. We conclude that this is related to the presence of fast modes which change the produced color. Therefore, obtaining a θ-independent color requires the elimination of the fast modes in the band diagram or, at least, limiting their intensity.

Suppression of unwanted modes to obtain angularly robust structural colors

Now, we will detail a procedure which allows us to erase the fast modes while keeping the slow ones; i.e. a procedure to get a band diagram with a flat band only, in the wanted wavelength range. We will demonstrate this method through an example, supposing that we want to produce, for E_y incident polarization, a θ-independent green color in reflection which corresponds to a flat band around 550 nm. We are looking for the best set of parameters (h, d, a_x, a_y) that achieves this goal. The first step is to consider a square lattice; the polarization is set and we plot the reflectivity under normal incidence using RCWA simulations as a function of the lattice period a and the wavelength λ for different heights and diameters until we get bands that cover a satisfactory wavelength range, as shown in Figure 8 (b), giving us a usable parameter couple (h,d). At this point, we do not know which of the bands visible in the reflectivity spectrum corresponds to the fast mode and which band corresponds to the slow mode. We therefore introduce an asymmetry in the lattice and we plot reflectivity spectra but, this time, varying a_x and a_y one by one, as shown in Figure 8 (c) for variations of a_y. This will allow us to differentiate the fast mode and the slow mode, thanks to their dependence on the lattice periods. Since we are using E_y polarization, Table 1 tells us that the slow mode is TM and that its spectral position depends on a_y, allowing us to label the modes (TE or TM) in the reflectivity diagrams of Figure 8 (b,c). Furthermore, we see on Figure 8 (c) that the slow mode (TM) occurs at wavelength 550 nm for a_y = 350 nm, and that the fast mode (TE) is indeed quasi-independent of the period a_y. Our goal is to reduce the intensity of the TE fast mode, which can be done by fixing a_x < 300 nm, such that the fast mode lies in the leakage-to-substrate window – opened by the structuration period in y – at the wavelength of interest of 550 nm (i.e., that at which the slow mode was positioned). For clarity, we have shown in Figure 8 (a) the domains corresponding to (i) modes exhibiting leakage by refraction to free space, (ii) modes exhibiting leakage by refraction to the substrate, and (iii) fully guided modes interacting by diffraction with waves in free space. The non-orthogonality of the TE and TM modes in the presence of the PCWG structure (indeed, both are excited in the structure using the same incident wave of a given polarization) means that they share the same loss channels, one of which being the leakage-to-substrate window induced by a structuration in the y direction. The effect of this leakage window on the intensity of the reflectivity peak linked to the TE fast mode is clearly visible in Figure 8 (c): the intensity of the fast mode (TE) feature falls sharply as the period increases beyond $\lambda/n_{substrate}$. A constrained parameter sweep using these rules as a starting point yields the best set of parameters (h = 150 nm, d = 200 nm, a_x = 250 nm, a_y = 350 nm). As expected, Figure 8 (e) shows that we now have only a flat band which, for θ < 40°, gives a relatively satisfying green. In this angular range, the TM slow mode dominates the reflectivity over the visible spectral domain, as confirmed by Figure 8 (g) and (h).

Thus, we detailed a method to get design parameters which produce the color we want with relatively little change as a function of the angle of observation. In the example, we set the polarization on E_y but this method is valid regardless of the desired polarization and color. For completeness, and to show the polarization dependent nature of the system, we show the reflectivities of the system for E_x polarized incident light during the optimization in Figure 8 (d) and for the final geometry in Figure 8 (f), where the latter shows the absence of strong reflection bands in this polarization.

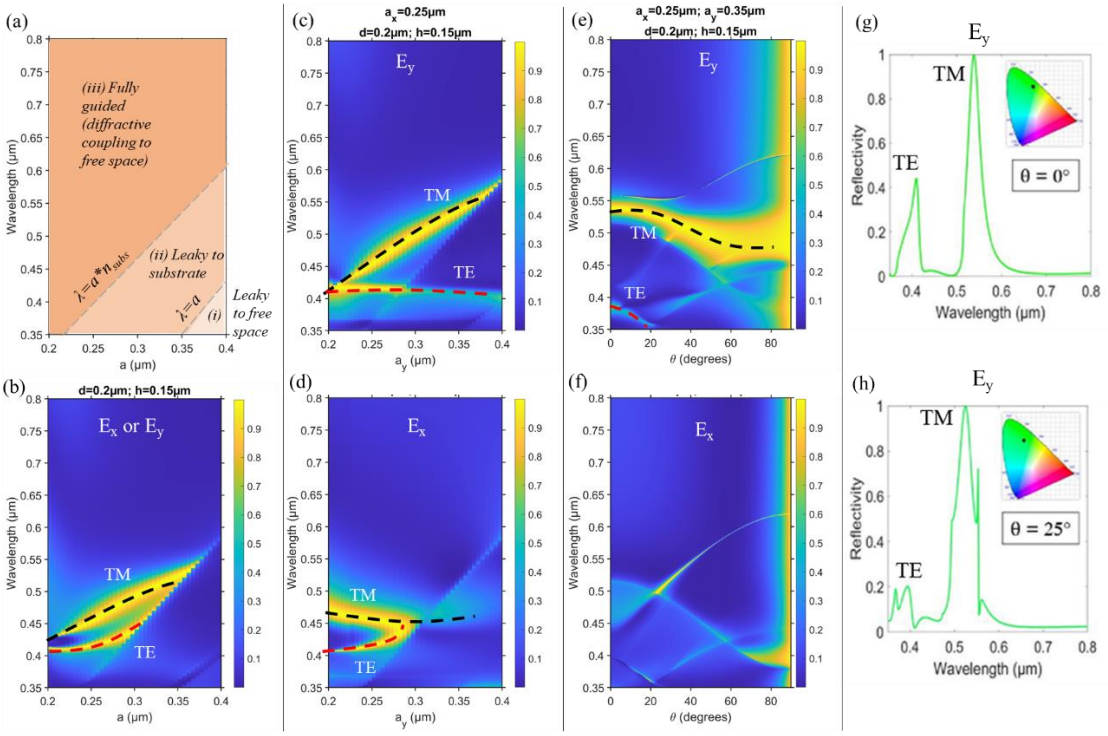

Figure 8 – (a) Reminder of identified regions in which reflection bands will occur with different confinement properties. (b) The reflectivity spectrum of a photonic crystals for a square lattice (valid in either E_x or E_y polarization), as a function of the wavelength and the lattice period. (c) The reflectivity spectrum of a photonic crystal for a rectangular lattice under E_y illumination. a_x is fixed and a_y is varied. (d) As c. but with E_x illumination. (e) The reflectivity spectra of the photonic crystal with specific parameters, chosen to produce a relatively monochromatic green under E_y illumination. (f) As e. but with E_x illumination. (g,h) The reflectivity spectra and CIE coordinates obtained for the green pixel under E_y illumination for θ = 0° and θ = 25° respectively.

In order to verify our system's robustness with respect to in-plane rotations (i.e. varying ϕ in the diagram shown in Figure 1), we have plotted in Figure 9 (a,b) the reflectivity as a function of ϕ for θ=0° (normal incidence) and θ=15° respectively. It can be seen that the flat band originally identified in Figure 8 still dominates the spectra, shown in Figure 9 (c), and displays only moderate wavelength drift indicating that the resulting color remains spectrally pure and relatively unchanged. This is confirmed quantitatively by the CIE chromaticity diagram in Figure 9 (d), where the plotted points correspond to variations in θ up to 25° and ϕ up to 15°.

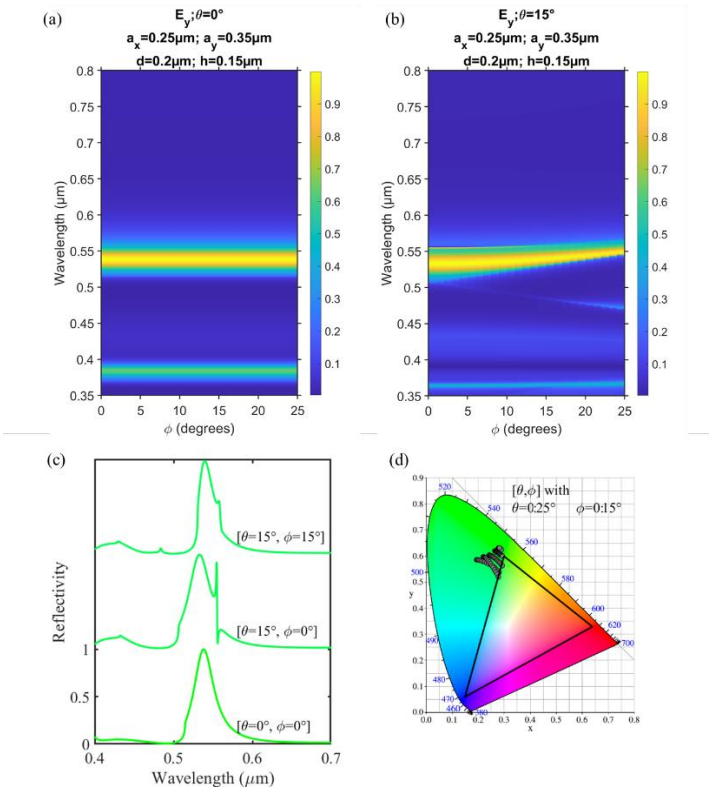

Figure 9 – Reflectivity of the PCWG structure optimized for green light under E_y illumination as a function of the rotation angle ϕ for (a) θ=0° and (b) θ=15°. (c) Reflectivity spectra for three pairs of (θ, ϕ) combinations as shown in the labels. (d) CIE chromaticity diagram showing points for (θ, ϕ) combinations in the ranges shown.

We underline that this technique makes it possible to realize colors which have the high spectral selectivity associated with PCWG structures that remain robust over a wide range of observation angles. However, it should be noted that such structures present a strong polarization dependence, that in the case of the above example optimized for green light under E_y illumination yields a much less intense reflection under E_x illumination, as can be seen by comparison of Figure 8 (e) and (f). In other words, if the system is illuminated with unpolarized light, it will respond as intended in reflection by delivering bright colors (reflectivities attaining near unity at the desired wavelengths) for half of the incident power (E_y polarized) and simply transmit the majority of the remaining power (E_x polarized). It will therefore still function efficiently in the reflectance regime as a color filter. In the following section, we will show how this polarization dependence can be exploited for color multiplexing applications.

Color multiplexing

After detailing the theory explaining color variations and their dependence on the polarization of light, we detail a possible application. Current color multiplexing methods often require complex nanostructures and instruments like mechanical stretching, chemical reaction or electronic control (16, 52,57,58,59). In this section, we detail a color multiplexing technique that does not need complex observation instruments, nor changes to the physical structure of the metasurface, just changes in the incident light polarization. Firstly, we need to introduce a new parameter given by $\eta = a_y/a_x$. For η = 1, the symmetry of the design leads to unchanged colors whatever the polarization considered, E_x or E_y. The asymmetry introduced by $\eta \neq 1$ allows us to create visual effects by changing the light polarization. Indeed, we saw in the precedent section that the band diagram of the metasurface varies with the polarization. One way to use this

property is to create different messages that can be only seen for one polarization or another. For this purpose, let us consider a picture separated into cells. Each cell (called "pixel" in the following) corresponds to a color i.e. to a set of nanopillars with identical parameters that we will color thanks to color palettes obtained by RCWA simulations for η greater and less than 1 (see Appendix). The goal here is to show the letters "INL" in E_x polarization which will become "NANO" in E_y polarization. For this purpose, we need four different types of pixels that cover all the possible behaviors of the photonic crystals submitted to light polarization. The color of the first type is unchanged regardless of the polarization considered. The color of the second type vary as a function of the polarization but is never dark. The third type of pixel is colored in E_x polarization and darkened in E_y polarization. Finally, the fourth type of pixel is colored in E_y polarization and darkened in E_x polarization. We will refer to them as type (i), (ii), (iii) and (iv) pixels, and their characteristics are summarized in Table 2. Figure 10 show different reflectivity spectra for each type of pixel in E_x and E_y polarization. We can notice that type (i) pixels are the easiest to design since they only require a square lattice to obtain a color which is not influenced by the light polarization.

Pixel type	*Characteristics*
(i)	Unsensitive to polarization
(ii)	Changes color for different polarizations
(iii)	Dark under E_y polarization, colored under E_x polarization
(iv)	Dark under E_x polarization, colored under E_y polarization

Table 2 – Characteristics of the four different pixel types.

By using the four types of pixels formerly described, we obtained the result shown in Figure 11. As expected, in E_x polarization, we can clearly see the letters "INL" and "NANO" in E_y polarization. The background is also composed of type (i) pixels of which color serves to make the darkened type (iii) and type (iv) pixels less visible since the color is not black but a very dark purple.

In order to determine the required pixel size, governing the number of repetitions of the unitary structure of the metasurface needed to produce the desired color through a collective resonance effect, we must consider a parameter referred to as the natural size of the modes, L (60). Whilst being beyond the scope of this paper, it can be shown that this parameter is given by multiplying the lifetime of photons by the mean group velocity of the mode that they inhabit giving a distance that can be assimilated to the interaction radius of light, hence giving the smallest required in-plane dimensions for the photonic crystal structure. Experimental work (2) on color printing with dielectric metasurfaces have shown robust colors in pixel with as few as 4 repetitions of a unit structure per side, giving a square pixel of around 1.5µm per side.

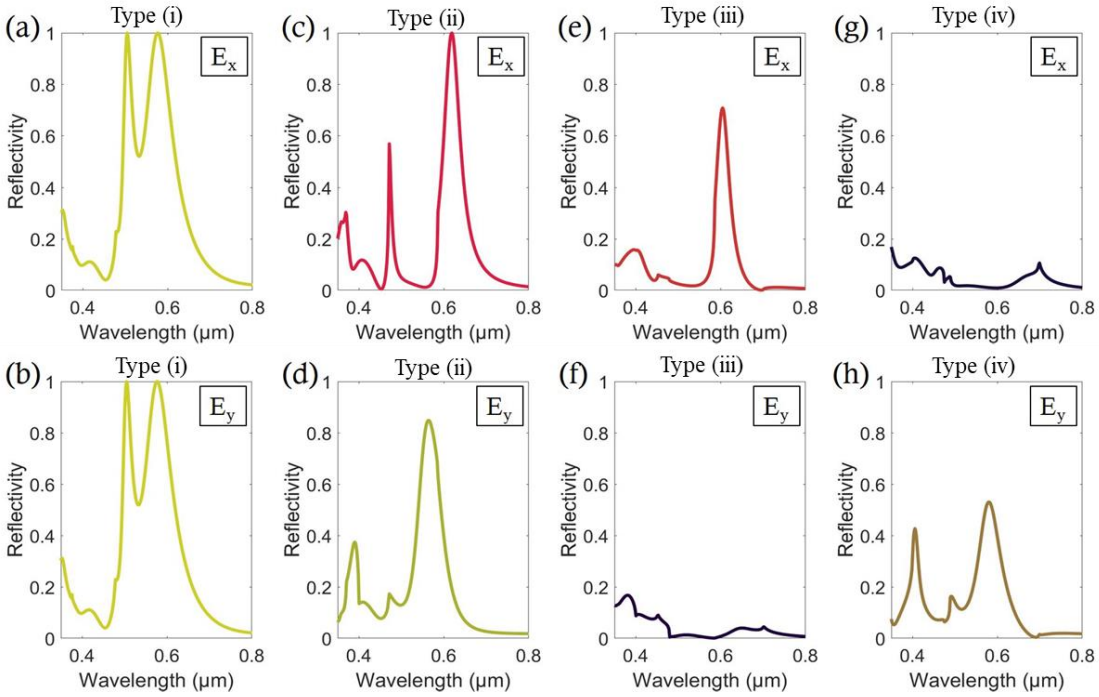

Figure 10 - (a)(b) The reflectivity spectra of a type (i) pixel in E_x and E_y polarization (a_x = 0.325μm, dc_x = 0.725, η = 1). (c)(d) The reflectivity spectra of a type (ii) pixel in E_x and E_y polarization (a_x = 0.325μm, dc_x = 0.8, η = 0.8). (e)(f) The reflectivity spectra of a type (iii) pixel in E_x and E_y polarization (a_x = 0.325μm, dc_x = 0.675, η = 1.4). (g)(h) The reflectivity spectra of a type (iv) pixel in E_x and E_y polarization (a_x = 0.475μm, dc_x = 0.45, η = 0.7).

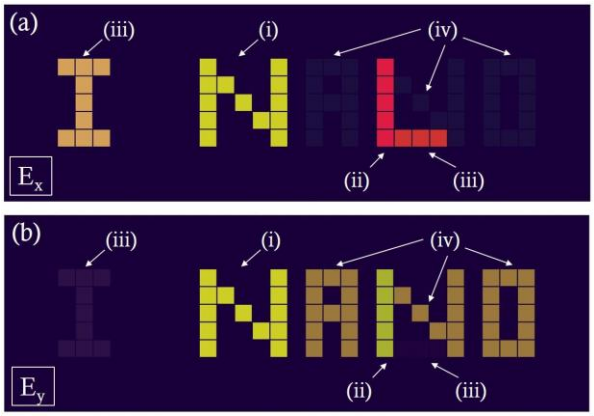

Figure 11 - (a) The image obtained in E_x polarization. (b) The image obtained in E_y polarization. The pixels' types are represented in both figures.

Conclusion

In conclusion, we realized an exhaustive study of the photonic crystals approach in the field of structural color after showing its main assets over the Mie resonators. Indeed, PCWGs are the most efficient since we have more parameters that allow us to control the color obtained in a precise way. Then, we described the behavior of photonic crystals through the study of band diagrams and detailed a method to limit the influence of the angle of observation on the color obtained, which is the main drawback of photonic crystal

structures. Finally, we detailed a color multiplexing technique which is only based on light polarization. The main perspective of this work is to implement angularly-resistant colors in color multiplexing. We note that the structures issued from the simulations presented are only optimized with respect to the parameters studied (namely the periods of the rectangular lattice and the height and diameter of the individual cylinders); as such, further improvements to the color-filtering performance of the systems presented may be expected if other properties of the system are added as degrees of freedom. These could include modifying the shape of individual resonators to further tune the symmetry properties of the PCWG, or the use of pillars made of different dielectric materials to suppress the multipolar modes in the TiO_2 metasurface via index matching (18,61). To conclude, the outcomes of this study have potential applications in the field of color displays and cryptography.

We acknowledge fundings from the French National Research Agency (ANR) under the project MetaOnDemand (ANR-20-CE24-0013).

Appendix

Figure 12 shows two examples of color palettes (one for each polarization, i.e. E_x and E_y) obtained with the color multiplexing technique presented in this work. It should be noted that these palettes are not the only ones accessible with the technique, as they require a certain number of parameters to be fixed, namely η and h. It can be seen that the pixels created cover a wide range of the CIE chromaticity space; filling and in some cases exceeding the RGB triangle.

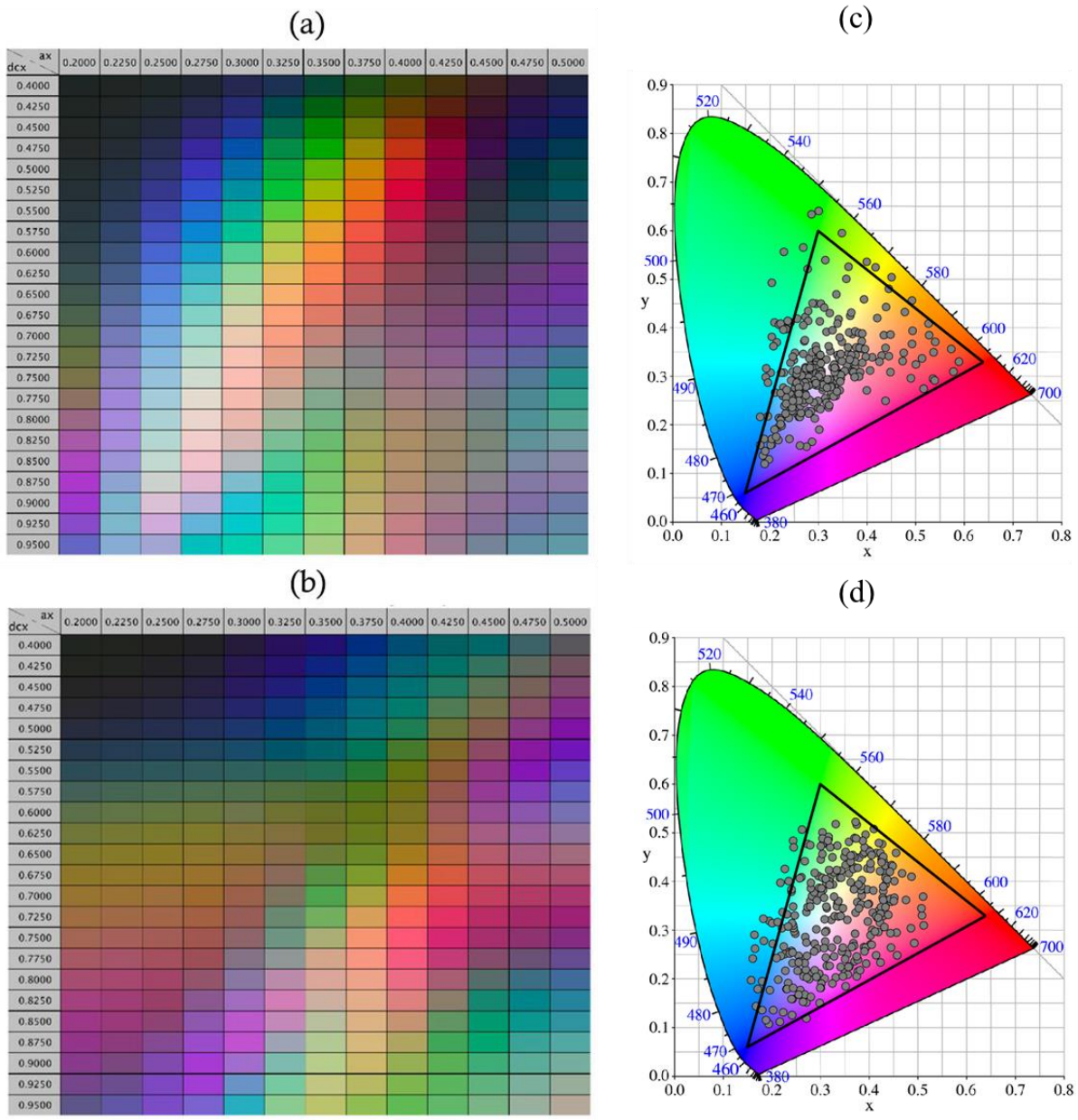

Figure 12 - (a) An example of color palette used in color multiplexing. Here, the parameters are h = 200nm, η = 0.6, θ = 0◦, in E_x polarization. a_x and $dc_x = d/a_x$ are the lattice period and the duty cycle along x-axis. (b) The same color palette in E_y polarization. (c,d) CIE chromaticity diagrams showing the placement of all of the colors shown in the palettes for E_x and E_y polarization respectively.

Supplementary Information

Further discussion of the reflectivity spectra presented in Figure 4.

Addition to results presented in Figure 6 to include E_y illumination.

For table of contents use only

"Design rules for structural colors in all-dielectric metasurfaces : from individual resonators to collective resonances and color multiplexing"

KÉVIN VILAYPHONE, MOHAMED AMARA, REGIS OROBTCHOUK, FABIEN MANDORLO, SERGE MAZAURIC, XAVIER LETARTRE, SÉBASTIEN CUEFF, HAI SON NGUYEN, AND THOMAS WOOD

Graphic showing the different systems studied in the paper, and their intrinsic advantages and drawbacks.

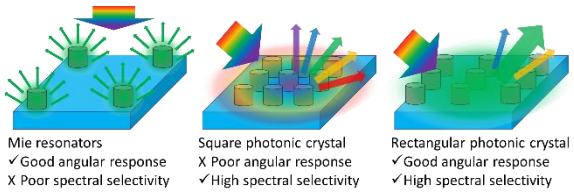

References

(1) J. Sun, B. Bhushan, and J. Tong, “Structural coloration in nature,” RSC Adv. 3, 14862 (2013).
(2) S. Sun, Z. Zhou, C. Zhang, Y. Gao, Z. Duan, S. Xiao, and Q. Song, “All-Dielectric Full-Color Printing with TiO2 Metasurfaces,” ACS Nano 11, 4445–4452 (2017).
(3) S. Checcucci, T. Bottein, M. Gurioli, L. Favre, D. Grosso, and M. Abbarchi, “Multifunctional Metasurfaces Based on Direct Nanoimprint of Titania Sol–Gel Coatings,” Adv. Opt. Mater. 7, 1801406 (2019).
(4) F. Gildas, Y. Dan, “Review of nanostructure color filters,” J. Nanophotonics, Vol 13(2), (2019).
(5) G. Yoon, T. Tanaka, T. Zentgraf, J. Rho, “Recent progress on metasurfaces: applications and fabrication,” J. Phys. D: Appl. Phys. 54 (2021).
(6) SD Rezaei, Z Dong, JYE Chan, J Trisno, RJH Ng, Q Ruan, C-W Qiu, NA Mortensen, JKW Yang, "Nanophotonic Structural Colors", ACS Photonics 8, 1, 18–33, 2021.
(7) W. Wang, D. Rosenmann, D. A. Czaplewski, X. Yang, and J. Gao, “Realizing structural color generation with aluminum plasmonic V-groove metasurfaces,” Opt. Express 25, 20454 (2017).
(8) A. S. Roberts, A. Pors, O. Albrektsen, and S. I. Bozhevolnyi, “Subwavelength Plasmonic Color Printing Protected for Ambient Use,” Nano Lett. 14, 783–787 (2014). Publisher: American Chemical Society.
(9) B. Zeng, Y. Gao, and F. J. Bartoli, “Ultrathin Nanostructured Metals for Highly Transmissive Plasmonic Subtractive Color Filters,” Sci. Reports 3, 2840 (2013).
(10) A. F. Kaplan, T. Xu, and L. Jay Guo, “High efficiency resonance-based spectrum filters with tunable transmission bandwidth fabricated using nanoimprint lithography,” Appl. Phys. Lett. 99, 143111 (2011).
(11) F. Cheng, J. Gao, T. Luk, and X. Yang, “Structural color printing based on plasmonic metasurfaces of perfect light absorption,” Sci. Reports 5 (2015).
(12) F. Cheng, J. Gao, L. Stan, D. Rosenmann, D. Czaplewski, and X. Yang, “Aluminum plasmonic metamaterials for structural color printing,” Opt. Express 23, 14552 (2015).
(13) F. Cheng, X. Yang, D. Rosenmann, L. Stan, D. Czaplewski, and J. Gao, “Enhanced structural color generation in aluminum metamaterials coated with a thin polymer layer,” Opt. Express 23, 25329 (2015).
(14) SN Chowdhury, P Nyga, ZA Kudyshev, EG Bravo, AS Lagutchev, AV Kildishev, VM Shalaev, A Boltasseva, "Lithography-Free Plasmonic Color Printing with Femtosecond Laser on Semicontinuous Silver Films", ACS Photonics 8, 2, 521–530, 2021.
(15) B. Yang, H. Cheng, S. Chen, and J. Tian, “Structural colors in metasurfaces: principle, design and applications,” Mater. Chem. Front. 3, 750–761 (2019).
(16) V.-C. Su, C. H. Chu, G. Sun, and D. P. Tsai, “Advances in optical metasurfaces: fabrication and applications (Invited),” Opt. Express 26, 13148 (2018).
(17) U. Zywietz, A. B. Evlyukhin, C. Reinhardt, and B. N. Chichkov, “Laser printing of silicon nanoparticles with resonant optical electric and magnetic responses,” Nat. Commun. 5, 3402 (2014).
(18) B. Yang, W. Liu, Z. Li, H. Cheng, D.-Y. Choi, S. Chen, and J. Tian, “Ultrahighly Saturated Structural Colors Enhanced by Multipolar-Modulated Metasurfaces,” Nano Lett. 19, 4221–4228 (2019).
(19) P. P. Iyer, N. A. Butakov, and J. A. Schuller, “Reconfigurable Semiconductor Phased-Array Metasurfaces,” ACS Photonics 2, 1077–1084 (2015).
(20) S. Jahani and Z. Jacob, “All-dielectric metamaterials,” Nat. Nanotechnol. 11, 23–36 (2016).
(21) A. Kuznetsov, A. Miroshnichenko, M. Brongersma, Y. Kivshar, and B. Luk’yanchuk, “Optically resonant dielectric nanostructures,” Science 354, (2016).
(22) V Flauraud, M Reyes, R Paniagua-Domínguez, AI Kuznetsov, J Brugger, "Silicon Nanostructures for Bright Field Full Color Prints", ACS Photonics 4, 8, 1913–1919, 2017.
(23) V Vashistha, G Vaidya, RS Hegde, AE Serebryannikov, N Bonod, M Krawczyk, "All-Dielectric Metasurfaces Based on Cross-Shaped Resonators for Color Pixels with Extended Gamut", ACS Photonics 4, 5, 1076–1082, 2017
(24) W Yang, S Xiao, Q Sing, Y Liu, Y Wu, S Wang, J Yu, J Han, D-P Tsai, All-dielectric metasurface for high-performance structural color. Nat Commun 11, 1864 (2020).
(25) H Liu, H Yang, Y Li, B Song, Y Wang, Z Liu, L Peng, H Lim, J Yoon, W Wu, Switchable All-Dielectric Metasurfaces for Full-Color Reflective Display, Adv Opt Mat 7, 8, 2019.
(26) P Huo, M Song, W Zhu, C Zhang, L Chen, H J Lezec, Y Lu, A Agrawal, T Xu, Photorealistic full-color nanopainting enabled by a low-loss metasurface, Optica Vol. 7, Issue 9, pp. 1171-1172 (2020).
(27) A K Gonzalez-Alcalde, A Reyes-Coronado, Large angle-independent structural colors based on all-dielectric random metasurfaces, Optics Communications Vol 475, 126289, 2020.
(28) B. Groever, W. T. Chen, and F. Capasso, “Meta-Lens Doublet in the Visible Region,” Nano Lett. 17, 4902–4907 (2017).
(29) M. Khorasaninejad, A. Y. Zhu, C. Roques-Carmes, W. T. Chen, J. Oh, I. Mishra, R. C. Devlin, and F. Capasso, “Polarization-Insensitive Metalenses at Visible Wavelengths,” Nano Lett. 16, 7229–7234 (2016).
(30) Q. Fan, D. Wang, P. Huo, Z. Zhang, Y. Liang, and T. Xu, “Autofocusing Airy beams generated by all-dielectric metasurface for visible light,” Opt. Express 25, 9285–9294 (2017).
(31) J. Balthasar Mueller, N. A. Rubin, R. C. Devlin, B. Groever, and F. Capasso, “Metasurface Polarization Optics: Independent Phase Control of Arbitrary Orthogonal States of Polarization,” Phys. Rev. Lett. 118, 113901 (2017).
(32) X. Fu, T. J. Cui, “Recent progress on metamaterials: From effective medium model to real-time information processing system,” Prog. in Quant. Electronics 67 (2019).
(33) T. Wood, M. Naffouti, J. Berthelot, T. David, J-B. Claude, L. Métayer, A. Delobbe, L. Favre, A. Ronda, I. Berbezier, N. Bonod, M. Abbarchi, “All-Dielectric Color Filters Using SiGe-Based Mie Resonator Arrays”, ACS Photonics, 4, 4, 873–883 (2017).
(34) J. A. Fan, C. Wu, K. Bao, J. Bao, R. Bardhan, N. J. Halas, V. N. Manoharan, P. Nordlander, G. Shvets, and F. Capasso, “Self-

Assembled Plasmonic Nanoparticle Clusters," Science 328, 1135–1138 (2010).
(35) F. J. García de Abajo, "Colloquium: Light scattering by particle and hole arrays," Rev. Mod. Phys. 79, 1267–1290 (2007).
(36) C. Genet and T. Ebbesen, "Light in tiny holes," Nature 445, 39–46 (2007).
(37) Y Shen, V Rinnerbauer, I Wang, V Stelmakh, JD Joannopoulos, M Soljačić, "Structural Colors from Fano Resonances", ACS Photonics 2, 1, 27–32, 2015.
(38) Z Liu, CH Lin, CW Sher, Z Lv B Luo, F Jiang, T Wu, CH H, HC Kuo, JH He, "Micro-light-emitting diodes with quantum dots in display technology", Light: Science and Applications 9:83, 2020.
(39) P Richner, P Galliker, T Lendenmann, SJP Kress, DK Kim, DJ Norris, D Poulikakos, "Full-Spectrum Flexible Color Printing at the Diffraction Limit", ACS Photonics 3, 5, 754–757, 2016.
(40) Z. Dong, L. Jin, S.D. Rezaei, H. Wang, Y. Chen, F. Tjiptoharsono, J. Ho, S. Gorelik, R.J.H Ng, Q. Ruan, C-W. Qiu, J. K. W. Yang, "Schrödinger's red pixel by quasi-bound-states-in-the-continuum", Science Advances, Vol 8, Issue 8, (2022).
(41) T Guo, J Evans, N Wang, S He, « Monolithic chip-scale structural color filters fabricated with simple UV lithography », Opt Exp Vol. 27, No. 15 , 2019.
(42) L Driencourt, F Federspiel, D Kazazis, L-T Tseng, R Frantz, Y Ekinci, R Ferrini, B Gallinet, « Electrically tunable multicolored filter using birefringent plasmonic resonators and liquid crystals », ACS Photonics, 7, 2, 444–453, 2020.
(43) L Li, S Shi, M Escuti, « Improved saturation and wide-viewing angle color filters based on multi-twist retarders », Opt Exp 29, No. 3, 2021.
(44) Y. Intaravanne, X. Chen, "Recent advances in optical metasurfaces for polarization detection and engineered polarization profiles," J. Nanophotonics, Vol 9(5), (2020).
(45) L. Wang, T. Li, R. Y. Guo, W. Xia, X. G. Xu, S. N. Zhu, "Active display and encoding by integrated plasmonic polarizer on light-emitting-diode", Scientific Reports volume 3, 2603 (2013)
(46) Yue, F., Zhang, C., Zang, XF. et al. High-resolution grayscale image hidden in a laser beam. Light Sci Appl 7, 17129 (2018).
(47) C. Zhang, D. Wen, F. Yue, Y. Intaravanne, W. Wang, X. Chen, "Optical Metasurface Generated Vector Beam for Anticounterfeiting", Phys. Rev. Applied 10, 034028, 2018,
(48) X Zang, F Dong, F Yue, C Zhang, L Xu, Z Song, M Chen, P-Y Chen, GS. Buller, Y Zhu, S Zhuang, W Chu, S Zhang, X Chen "Polarization Encoded Color Image Embedded in a Dielectric Metasurface", Adv. Mater. 1707499, 2018.
(49) Zhao, R., Sain, B., Wei, Q. et al. "Multichannel vectorial holographic display and encryption", Light Sci Appl 7, 95 (2018)
(50) C Zhang, F Dong, Y Intaravanne, X Zang, L Xu, Z Song, G Zheng, W Wang, W Chu, X Chen, "Multichannel Metasurfaces for Anticounterfeiting", Phys. Rev. Applied 12, 034028, 2019.
(51) L Wang, T Wang, R Yan, X Yue, H Wang, Y Wang, J Zhang, X Yuan, J Zeng, J Wang, Color Printing and Encryption with Polarization-Switchable Structural Colors on All-Dielectric Metasurfaces, Nano Lett. 23, 12, 5581–5587, 2023.
(52) P. Gutruf, C. Zou, W. Withayachumnankul, M. Bhaskaran, S. Sriram, and C. Fumeaux, "Mechanically Tunable Dielectric Resonator Metasurfaces at Visible Frequencies," ACS Nano 10, 133–141 (2016).
(53) T. Smith and J. Guild, "The C.I.E. colorimetric standards and their use," Transactions Opt. Soc. 33, 73–134 (1931).
(54) Editor Popov E, "Gratings: Theory and Numeric Applications, Second Revisited Edition", ISBN: 2-85399-943-4 (2014)
(55) Paniagua-Dominguez R, Yu YF, Miroshnichenko AE, Krivitsky LA, Fu YH, Valuckas V, Gonzaga L, Toh YT, Kay AYS, Luk'yanchuk B, Kuznetsov AI, "Generalized Brewster effect in dielectric metasurfaces", NatComms, 7:10362 (2016).
(56) Babicheva VE, Evlyukhin AB, "Resonant Lattice Kerker Effect in Metasurfaces With Electric and Magnetic Optical Responses", Laser Photonics Rev. 1700132 (2017).
(57 H.-T. Chen, A. J. Taylor, and N. Yu, "A review of metasurfaces: physics and applications," Reports on Prog. Phys. 79, 076401 (2016).
(58) J. Sautter, I. Staude, M. Decker, E. Rusak, D. N. Neshev, I. Brener, and Y. S. Kivshar, "Active Tuning of All-Dielectric Metasurfaces," ACS Nano 9, 4308–4315 (2015).
(59) C. Yang, Y. Luo, J. Guo, Y. Pu, D. He, Y. Jiang, J. Xu, and Z. Liu, "Wideband tunable mid-infrared cross polarization converter using rectangle-shape perforated graphene," Opt. Express 24, 16913–16922 (2016).
(60) X. Letartre, J. Mouette, J. L. Leclercq, P. Rojo Romeo, C. Seassal, P. Viktorovitch, "Switching Devices with Spatial and Spectral Resolution Combining Photonic Crystal and MOEMS Structures", J. Lightwave Technology, Vo. 21, No. 7, (2003).
(61) K. Baek, Y. Kim, S. Mohd-Noor, and J. K. Hyun, "Mie Resonant Structural Colors," ACS Appl. Mater. Interfaces 12, 5300–5318 (2020).